PORE-SCALE COMPUTATION OF MATERIAL AND TRANSPORT PROPERTIES ON NORTH-SEA RESERVOIR ROCKS

P.-E. ØREN[1], S. BAKKE[1], R.J. HELD[2]

[1]Numerical Rocks AS, N-7041 Trondheim, Norway
[2]Statoil ASA, N-7005 Trondheim, Norway

Abstract

This work investigates complex sandstone lithofacies in a North-Sea petroleum reservoir field. We compare samples acquired by X-ray microtomography with digitized samples of reconstructed lithofacies. The study largely shows an excellent agreement of directly calculated effective properties and shows that the reconstructed samples reproduce important effective properties for these heterogeneous rock types. Our results allow interpretation of trends in effective medium properties and construction of cross-property relations for the investigated lithofacies.

1. INTRODUCTION

In recent years, several direct (e.g., Arns et al., 2004) and reconstruction based techniques (e.g., Øren and Bakke, 2002) have been established for the acquisition of digitized representations of rock microstructures. The availability of these data allow direct prediction of effective properties based on digitized pore structure information. Effective properties that can be numerically calculated include elastic moduli, electrical resistivities, fluid permeabilities, and constitutive relationships for multiphase flow.

We compare two different techniques, one direct and one reconstruction based, for the three-dimensional digitization of realistic pore structures. The direct technique is a standard application of X-ray tomography at high resolutions; the resolution of the tomographic data presented herein is 5.24 μm for an extracted sample size of 1 cm in diameter. The tomographic images were obtained from the Australian National University.

The reconstruction based technique is an explicit simulation of geological rock-forming processes, i.e., sedimentation, compaction, and diagenetic overprinting. Input parameters for the reconstruction are extracted from backscattered electron (BSE) images of 2D thin sections. A detailed description of the applied procedures and the predictive capabilities is given elsewhere (Bakke and Øren, 1997; Øren et al., 1998; Øren and Bakke, 2002).

2. SAMPLE CHARACTERIZATION

The presented reservoir rock examples are poorly consolidated sandstones with an average grain size diameter between 140 $\mu\text{m} < d < 900$ μm, a porosity ϕ of 0.23 to 0.27, and a permeability range between 1 and 10 Darcy. The depositional environment constitutes that of a fluvial channel setting. Hence the samples are heterogeneous and have in addition undergone complex diagenetic alteration, i.e., formation of authigenic clay minerals and

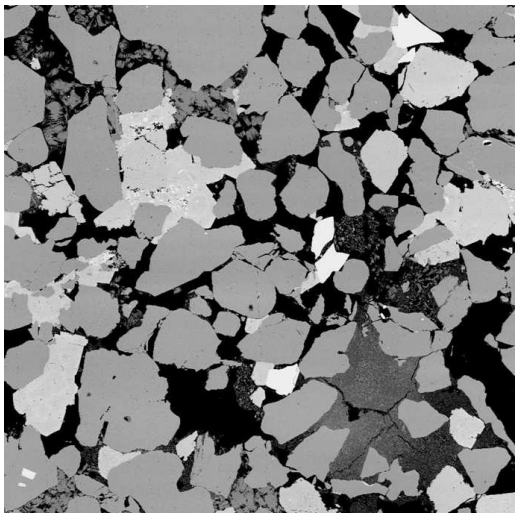

FIGURE 1. BSE image for a heterogeneous North Sea reservoir sandstone, indicating pore space (black), clay (dark gray), quartz (gray), feldspar (lighter gray) and carbonate cement (light gray). The pixel resolution is 3.31 μm and the side length of the image is 2.68 mm.

patchy carbonate cementation (see Figure 1). Additional Special Core Analysis information for the rock type is available, including capillary pressure and relative permeability measurements. The porosity obtained from BSE imaging is 0.236. A mosaic of 256 of such images from a thin section was employed as input for the sample reconstruction.

Cross-sections of the microtomographic image, denoted MCT, and the reconstructed sample, denoted PBM, are compared in Figure 2. Both samples are voxel-based with a size of 512^3. In the following, we compute and compare important morphological and effective material and transport properties of these samples. Core plug measurements are given where they are available.

2.1. **Morphological Measures.** A quantitative microstructural characterization is fundamental for determining and predicting effective properties of heterogeneous porous media, such as reservoir rocks. In a discretized porous medium, the disjoint sets of pore space and matrix can be described via an indicator function $I(\mathbf{x})$, where $\mathbf{x}$ is a position vector. $I(\mathbf{x}) = 1$, if $\mathbf{x} \in$ pore space, and $I(\mathbf{x}) = 0$ otherwise. The porosity is then defined as the statistical average $\phi = \langle Z(\mathbf{x}) \rangle$. Angular brackets denote here volumetric averaging. The two-point correlation function $C_2(\mathbf{u})$ is calculated from the indicator function as

$$C_2(\mathbf{u}) = \frac{\langle (I(\mathbf{x}) - \phi) \cdot (I(\mathbf{x}+\mathbf{u}) - \phi) \rangle}{\phi(1-\phi)} \tag{1}$$

and measures the probability of finding the two end points of a segment of length $\mathbf{u}$ within the same phase. We computed the two-point correlation function for $\mathbf{u}$ aligned with the coordinate axes and performed directional averaging. $C_2(\mathbf{u})$ provides information about spatial correlation scales in the microstructure.

The lineal path function $L^{(\alpha)}(z)$ measures the probability that a line segment of length z lies entirely in phase α. The lineal path function is monotonically decreasing with z, and

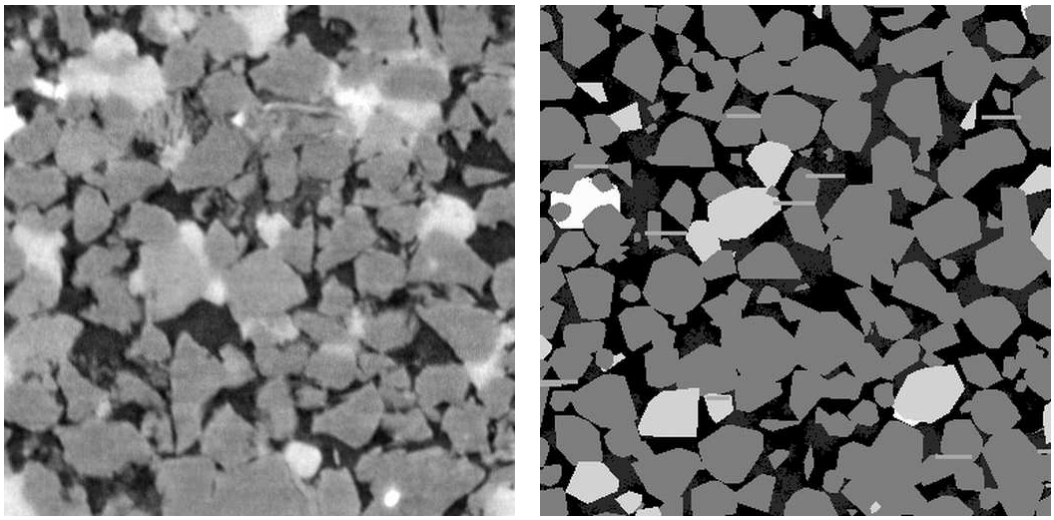

FIGURE 2. MCT image (left) and PBM reconstruction (right) for a heterogeneous North Sea reservoir sandstone, indicating pore space (black), clay (dark gray), quartz (gray), feldspar and mica (light gray), and carbonate cement (white). Side length of the images is 2.68 mm.

normalized by porosity yields $L^{(\alpha)}(0) = 1$ and $L^{(\alpha)}(\infty) = 0$. The tail of $L^{(\alpha)}(z)$ provides information about the largest pore or matrix lengths.

Local porosity distributions (Hilfer, 1991; Biswal et al., 1998) measure the probability of finding the local porosity ϕ in the range $\phi \pm \Delta\phi$. Let $\phi(\mathbf{x}, L) = \langle I(\mathbf{x}) \rangle_{\mathcal{M}}$ be the porosity of a cubic measurement cell $\mathcal{M}(\mathbf{x}, L)$ of side length L centered at position $\mathbf{x}$, then

$$\mu(\phi, L) = \frac{1}{m\Delta\phi} \sum_{\mathbf{x}} \delta_\phi(\phi - \phi(\mathbf{x}, L)) \tag{2}$$

where m is the number of placements of the measurement cell $\mathcal{M}(\mathbf{x}, L)$ and the indicator $\delta_\phi = 1$, if $\mid \phi - \phi(\mathbf{x},\mathrm{L})| \leq \Delta\phi$, and $\delta_\phi = 0$ otherwise. We calculated $\mu(\phi, L)$ by placing $\mathcal{M}(\mathbf{x}, L)$ at all voxels which are at least a distance $L/2$ from the sample boundaries.

Local percolation probabilities provide a quantitative characterization of the connectivity of the pore space (Hilfer, 1991; Biswal et al., 1998). A measurement cell $\mathcal{M}(\mathbf{x}, L)$ percolates in the i-direction if there exists a continuous path inside the pore space that connects the inlet and outlet face. Let $\Lambda_i(\mathbf{x}, L)$ be an indicator of percolation with $\Lambda_i(\mathbf{x}, L) = 1$ if $\mathcal{M}(\mathbf{x}, L)$ percolates, and $\Lambda_i(\mathbf{x}, L) = 0$ otherwise. The total fraction of all cells of size L that percolate in a given direction i ($i = x, y, z$) is determined by

$$P_i(L) = \frac{1}{m} \sum_{\mathbf{x}} \Lambda_i(\mathbf{x}, L) \tag{3}$$

$P_i(L)$ is an important characteristic of pore networks, i.e., it quantifies the fraction of pore elements that are open to flow.

2.2. **Transport Properties.** Averaging of local equations relates the effect of the microstructure to effective physical transport properties applicable at the macroscopic scale. For local transport properties in homogeneous media, a generalized flux (associated with a

conservable quantity such as electrical current, stress, or momentum) is linearly related to a generalized gradient (electrical field, strain, pressure) with the proportionality constant $\mathcal{K}_e$. For elasticity and electrical conduction, this may be written as $\mathcal{F}(\mathbf{x}) = K_e(\mathbf{x}) \cdot \mathcal{G}(\mathbf{x})$, where $\mathcal{F}$ obeys the differential equation $\nabla \cdot \mathcal{F}(\mathbf{x}) = 0$

In heterogeneous media, we expect similar linear constitutive relations involving averaged fields

$$\begin{aligned} [\mathcal{F}(\mathbf{x})] &= \mathcal{K}_e \cdot [\mathcal{G}(\mathbf{x})] \qquad \text{and} \\ [\mathbf{v}(\mathbf{x})] &= \mathcal{K}_e \cdot g(\mathbf{x}) \qquad \text{with} \quad \mathcal{K}_e = -k/\mu \end{aligned} \tag{4}$$

for elasticity/conductivity and permeability, respectively. Angular brackets denote an average operation such that $\mathcal{K}_e$ becomes the effective property. $\mathbf{v}$ denotes fluid velocity, g is an applied pressure gradient, k is absolute permeability, and μ is fluid viscosity.

The local equations that govern the elastic behaviour of the heterogeneous medium are the basic equations of elastostatics,

$$\nabla \cdot \tau = 0 \tag{5}$$

$$\tau = \mathbf{C} : \varepsilon \qquad \text{with} \quad \varepsilon = \frac{1}{2}\left[\nabla \mathbf{d} + (\nabla \mathbf{d})^T\right] \tag{6}$$

where τ and ε denote the stress and strain tensors, respectively, $\mathbf{d}$ is the displacement field, and $\mathbf{C}$ is the stiffness tensor. The above equations were solved via a finite element method using an energy representation of the linear elastic equations. Periodic boundary conditions are imposed on the faces of the digital images. The effective bulk and shear moduli are computed assuming isotropic linear elastic behaviour.

For the steady state conductivity problem, the governing local equations become the Laplace equation,

$$\nabla \cdot \mathbf{J} = 0 \tag{7}$$

$$\mathbf{J} = \sigma^{(w)} \nabla \Phi \tag{8}$$

subject to the boundary condition $\nabla \Phi \cdot \mathbf{n} = 0$ on the solid walls. Here $\mathbf{J}$ is the electrical current, $\sigma^{(w)}$ is the electrical conductivity of the fluid in the pore space, Φ is the potential or voltage, and $\mathbf{n}$ is the unit vector normal to the solid wall. Numerical solutions of the Laplace equation were obtained by a finite difference method. The directional conductivities σ_i are computed by applying a potential gradient across the medium and imposing no flow boundary conditions laterally. A directional formation factor F_i is defined as the inverse of the effective electrical conductivity, $F_i = \sigma^{(w)}/\sigma_i$. The average formation factor $\bar{F}$ is a harmonic mean of the direction dependent formation factors.

The low Reynolds number flow of an incompressible Newtonian fluid is governed by the steady state Stokes equations

$$\mu \nabla^2 \mathbf{v} = \nabla p, \tag{9}$$

$$\nabla \cdot \mathbf{v} = 0 \tag{10}$$

subject to the boundary condition $\mathbf{v} = 0$ on the solid walls. $\mathbf{v}$, p, and μ are the velocity, pressure, and fluid viscosity, respectively. A D3Q19 Lattice Boltzmann algorithm (Jin et al., 2004) was used to numerically solve the Stokes equations on the digitized images. The directional absolute permeabilities k_i are determined by applying a pressure difference Δp

along the i-axes. The macroscopic flux is then given by volumetric averaging of the local fluid velocity and k_i is determined from Darcy's law. The effective absolute permeability $\bar{k}$ is given by the arithmetic average of the directional permeabilities.

3. RESULTS

3.1. **Correlation and lineal path functions.** The two-point correlation and the lineal path functions for the MCT and PBM pore structures are in good agreement (see Figure 3). The presented functions are an average of the directional functions. The initial slope of C_2 allows an estimation of the specific surface areas (Yeong and Torquato, 1998) with 0.0205 μm^{-1} and 0.0192 μm^{-1} for the MCT and PBM samples, respectively. The decay length, determined at $C_2 = 0$, is found with $L \simeq 0.72$ mm in both cases. The tail in C_2 and similarly in $L^{(\alpha)}(z)$ indicates a longer range structure in the samples. This is attributed to the wide grain size distribution and occurrence of clays and carbonate cementation.

3.2. **Local porosity distribution.** Local porosity distributions $\mu(\phi, L)$ for the two samples shown in Figure 4 are equally similar. The calculations give a characteristic length of $L = 0.39$ mm. Notable is the difference in the samples at $\mu(0, L)$, otherwise the width (variance in porosity) and peak (most probable porosity) of the distributions are comparable. The higher value at the origin for the reconstructed sample indicates that larger regions of matrix occur more frequently.

3.3. **Local percolation probability.** The local percolation probabilities are a sensitive measure of the connectivity of the pore structure that is of importance for flow and transport properties. The plot in Figure 4 represents the total fraction of cells that percolate in all three directions. The local percolation probabilities are similar for both samples, and diverge only at large L. However, the discrepancies are in our experience small. The intrinsic connectivity of the pore structure in the tomographic data is thus found adequately reproduced by the reconstruction process.

3.4. **Elastic properties.** The calculation of the bulk and shear moduli are presented in Figure 5. These results were obtained by simulation on non-overlapping subsamples. The side lengths of the cubic subsamples were 0.67 mm and 1.34 mm and thus in the range of the determined correlation lengths scales of the samples ($L \simeq 0.72$ mm for $C_2 = 0$). The trends plotted against porosity are near-linear, with a larger scatter at higher porosities. A difference in slope is apparent between the MCT and the PBM data. This yields a small, but systematic underprediction of the elastic moduli for the reconstructed image, or vice versa an overprediction in the tomographic image. The elastic moduli depend strongly on the representation of the grain to grain contacts. Whether the influence of image processing, i.e., thresholding, in the MCT sample accounts for this effect is not determined, yet we have indications supporting such interpretation.

3.5. **Conductive properties.** The results of the electrical conductivity calculations are shown in Figure 6. The reconstructed sample supports slightly higher conductances, or predicts lower formation factors, than the microtomographic image. A possible explanation might be found in the explicit accounting of small pores in the PBM sample that contribute significantly to the electrical conductance. The directional and averaged formation factors for the entire sample sizes are compiled in Table 1.

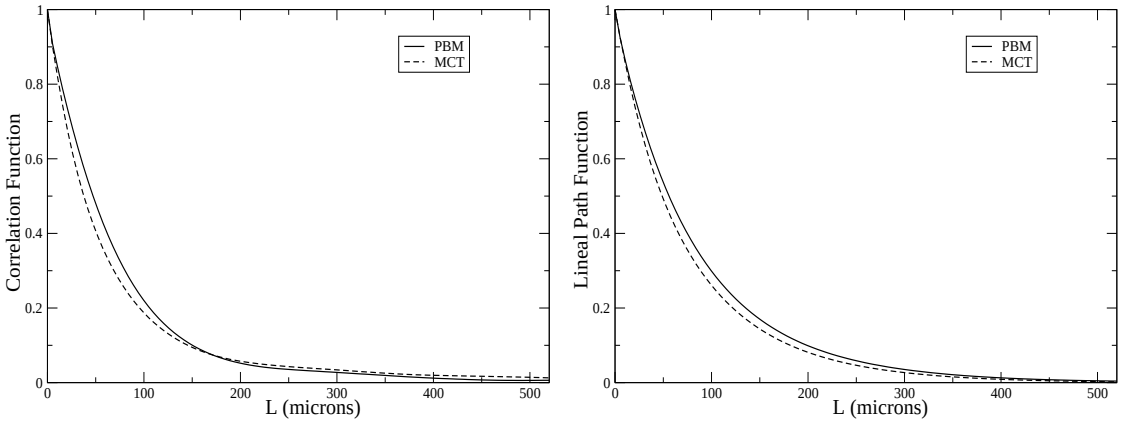

FIGURE 3. Average two-point correlation function $C_2(\mathbf{u})$ (left) and lineal path function $L^{(\alpha)}(z)$ (right) for the MCT and PBM samples.

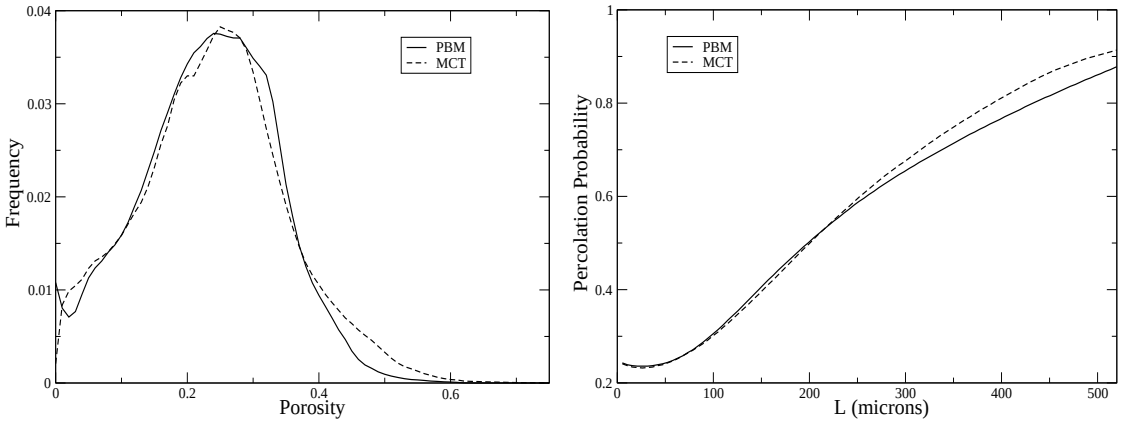

FIGURE 4. Local porosity distributions $\mu(\phi, L)$ (left) and local percolation probabilities $\lambda(L, \phi)$ (right) for MCT and PBM samples.

3.6. **Flow properties.** Results of the absolute permeability calculations are displayed in Figure 6. Results are shown again for subsamples of size 128^3 and 256^3 and indicate the variability contained in each sample. The observed trend in absolute permeability versus porosity is as expected and similar for both the reconstructed and the mircotomography pore structure. Absolute permeability calculations for the entire sample size of 512^3 are found in Table 1. These values can be compared with the absolute permeability measurement of 4370 mD on the larger core plug.

3.7. **Cross-property relations.** It is often desired to find relationships between different physical properties. Such cross-property relationships become especially useful if one property is more readily obtained than another property. Of particular interest are the link between the fluid permeability k and effective diffusion parameters, such as the effective conductivity σ, or the link between the effective elastic moduli and the effective conductivity. Figure 7 displays strong correlations between conductivity and bulk modulus/permeability based on pore-scale computations.

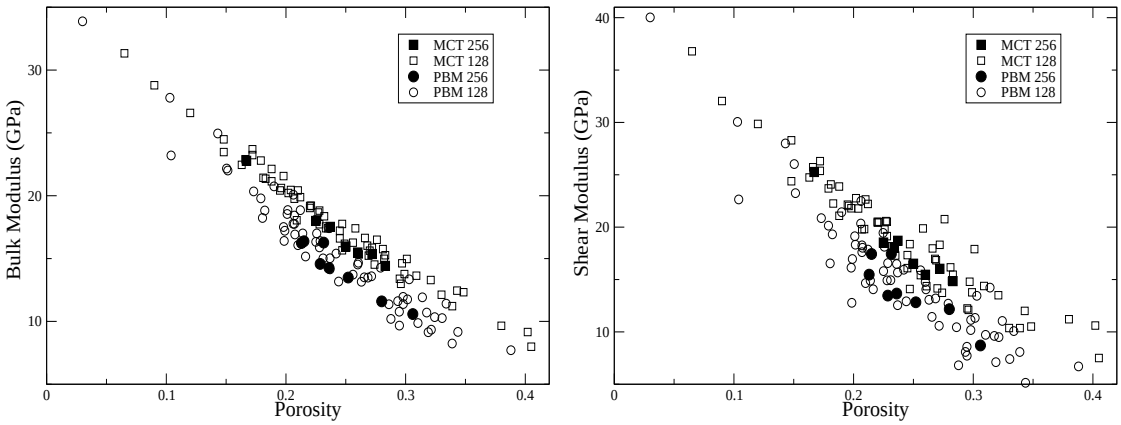

FIGURE 5. Bulk modulus (left) and shear modulus (right) versus porosity for the MCT and PBM samples. Shown are calculations on subsamples of size 128^3 and 256^3.

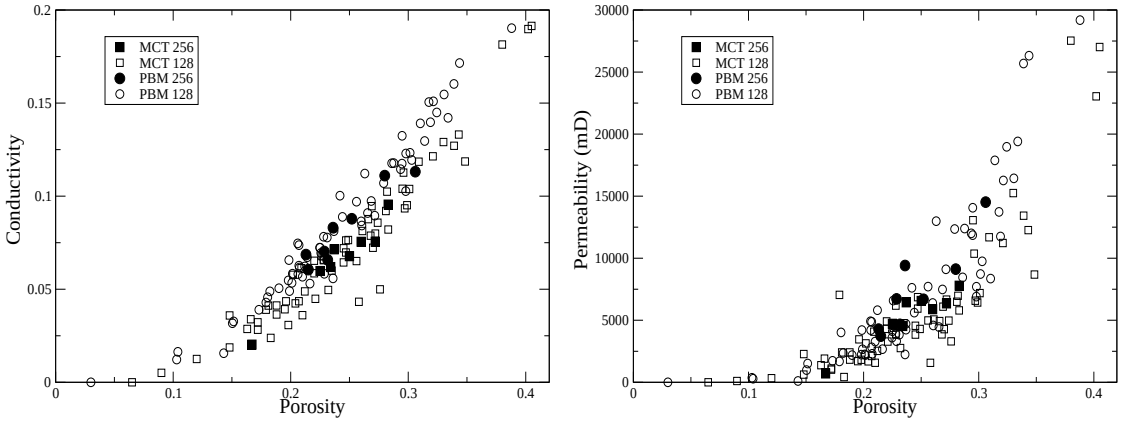

FIGURE 6. Electrical conductivity (left) and absolute permeability (right) versus porosity for the MCT and PBM samples. Shown are calculations on subsamples of size 128^3 and 256^3.

TABLE 1. Computed transport properties for the samples

Sample	ϕ	F_x	F_y	F_z	$\bar{F}$	k_x (mD)	k_y (mD)	k_z (mD)	$\bar{k}$ (mD)
MCT	0.240	12.7	16.6	12.2	13.6	5853	4322	6334	5503
PBM	0.243	10.8	10.9	11.0	10.9	6515	6132	6015	6221

4. DISCUSSION

We investigated the predictive capabilities of direct pore-scale simulations of elastic, electrical and transport related effective medium properties for a heterogeneous channel sandstone in a North Sea field. The study of these and other not included samples largely reveals an excellent agreement of the effective properties for microtomographic images and reconstructed samples for these heterogeneous rock types. Instances of deviation can

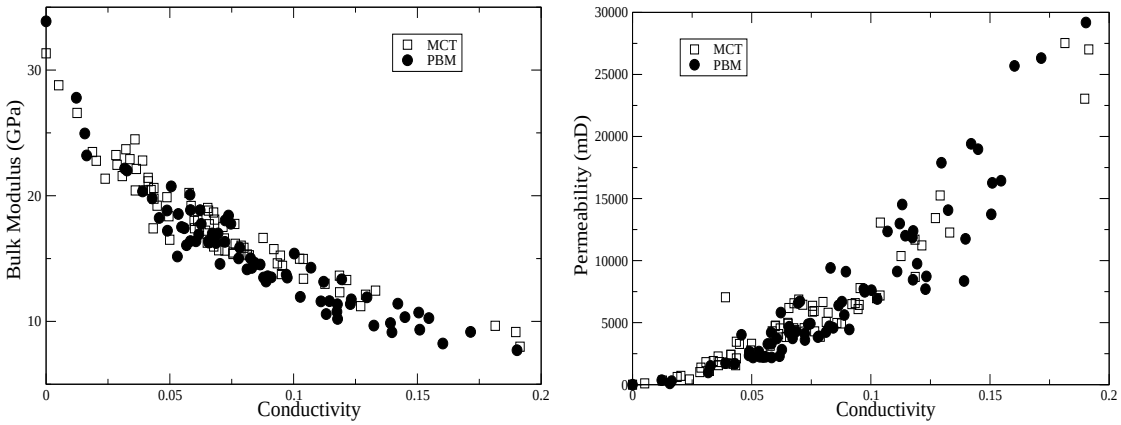

FIGURE 7. Cross-property correlations for conductivity against bulk modulus (left) and absolute permeability (right).

be attributed in other rock types to microstructural discrepancies, for example due to the resolution and processing of MCT data.

Our results demonstrate the feasibility of combining digitized pore structure data with numerical calculations to predict rock properties over a wide range of porosity and to derive cross-property correlations. This can lead to the development of type-curves for properties and cross-property relations for selected lithofacies, that are more readily constructed numerically than by experimentation.

As outlook on forthcoming work, the study of the effects of pore structure and wettability characteristics for the prediction of multiphase flow properties is ongoing. This requires the extraction of a representative pore network and simulation of pore-scale displacement mechanisms. The tools for such investigation are already in place.

REFERENCES

Arns, C.H., M.A. Knackstedt, V.W. Pinczewski, and N.S. Martys (2004), Virtual permeametry on microtomographic images, *J. Petroleum Science and Engineering*, 45, 41–46.

Bakke, S., and P.E. Øren (1997), 3-D pore-scale modelling of sandstones and flow simulations in the pore networks, *SPE Journal*, 2, 136–149.

Biswal, B., C. Manwarth, and R. Hilfer (1998), Three-dimensional local porosity analysis of porous media, *Physica A*, 255, 221–241.

Hilfer, R. (1991), Geometric and dielectric characterization of porous media, *Physical Review B*, 60–75.

Jin, G., T.W. Patzek, and D.B. Silin (2004), Direct predicition of the absolute permeability of unconsolidated and consolidated reservoir rock, *SPE Paper* 90084.

Yeong, C.L.Y., and S. Torquato (1998), Reconstructing random media, *Physical Review E*, 57, 495–506.

Øren, P.E., and S. Bakke (2002), Process based reconstruction of sandstones and predictions of transport properties, *Transport in Porous Media*, 46, 311–343.

Øren, P.E., S. Bakke, and O.J. Arntzen (1998), Extending predictive capabilities to network models, *SPE Journal*, 3, 324–336.